

See discussions, stats, and author profiles for this publication at: <https://www.researchgate.net/publication/231275852>

Photodissolution of iron oxides. 3. Interplay of photochemical and thermal processes in maghemite/carboxylic acid systems

ARTICLE *in* ENVIRONMENTAL SCIENCE AND TECHNOLOGY · NOVEMBER 1991

Impact Factor: 5.33 · DOI: 10.1021/es00023a011

CITATIONS

26

READS

20

4 AUTHORS, INCLUDING:



Marta I Litter

Comisión Nacional de Energía Atómica

144 PUBLICATIONS **4,619** CITATIONS

SEE PROFILE



Miguel A Blesa

Comisión Nacional de Energía Atómica

227 PUBLICATIONS **4,043** CITATIONS

SEE PROFILE

—would suggest that it was not readily degraded under such conditions. Whereas the quinone itself was not present in the sediment sample, the hydroquinone was recovered at a concentration of 0.9 mg/kg organic matter compared with a value of 207 mg/kg organic matter for the sum of all the chlorophenolic compounds extracted under identical conditions. The recovery of the hydroquinone is consistent with either (i) the observed water-sediment partition or (ii) reduction of the quinone under the highly anaerobic conditions in the sediment.

(ii) The pathway whereby the quinone is formed from aromatic precursors in lignin is unknown although 2,5-dichloro-3,6-dihydroxybenzo-1,4-quinone might be formed by reactions with chlorine dioxide analogous to those which produce 2-chloro-5-methoxybenzo-1,4-quinone from vanillyl alcohol or 2-methoxybenzo-1,4-quinone from 1'-methylvanillyl alcohol (17).

Conclusions

2,5-Dichloro-3,6-dihydroxybenzo-1,4-quinone has been identified in a number of different kinds of kraft mill bleaching effluents in concentrations comparable with those of currently dominant individual chloroguaiacols and chlorocatechols. Although its persistence in the environment has not been established, its low toxicity and its chemical properties do not suggest that on the basis of current evidence it would present a conspicuous environmental hazard.

Acknowledgments

We thank Åke Lundberg for the AOX analyses and Ulrika Wallin for the Microtox value.

Registry No. CAH₂, 123-31-9; CA, 87-88-7; 2,5-dichloro-3,6-dimethoxybenzo-1,4-quinone, 7210-71-1; 1,2,4,5-tetraacetoxy-3,6-dichlorobenzene, 135646-90-1; 1,4-diacetoxy-2,5-dichloro-3,6-dimethoxybenzene, 135646-91-2; tetrachloroguaiacol acetate, 85430-24-6; 4,5-dichloroguaiacol, 2460-49-3; 3,4,5-trichloroguaiacol, 57057-83-7; tetrachloroguaiacol, 2539-17-5; 3,4-dichlorocatechol,

3978-67-4; 3,4,5-trichlorocatechol, 56961-20-7; tetrachlorocatechol, 1198-55-6; quinone, 106-51-4.

Literature Cited

- (1) Kringstad, K. P.; Lindström, K. *Environ. Sci. Technol.* **1984**, *18*, 236A.
- (2) Neilson, A. H.; Allard, A.-S.; Hynning, P.-Å.; Remberger, M. *Toxicol. Environ. Chem.* **1991**, *30*, 3.
- (3) Remberger, M.; Allard, A.-S.; Neilson, A. H. *Appl. Environ. Microbiol.* **1986**, *51*, 552.
- (4) Remberger, M.; Hynning, P.-Å.; Neilson, A. H. *Environ. Toxicol. Chem.* **1988**, *7*, 795.
- (5) Allard, A.-S.; Hynning, P.-Å.; Remberger, M.; Neilson, A. H. *Appl. Environ. Microbiol.* **1991**, *57*, 77.
- (6) Martinsen, K.; Kringstad, A.; Carlberg, G. E. *Water Sci. Technol.* **1988**, *20*(2), 13.
- (7) Remberger, M.; Hynning, P.-Å.; Neilson, A. H. *J. Chromatogr.* **1990**, *508*, 159.
- (8) Das, B. S.; Reid, S. G.; Betts, J. L.; Patrick, K. J. *Fish. Res. Board Can.* **1969**, *26*, 3055.
- (9) Remberger, M.; Hynning, P.-Å.; Neilson, A. H. *Ecotoxicol. Environ. Saf.*, in press.
- (10) Neilson, A. H.; Allard, A.-S.; Hynning, P.-Å.; Remberger, M.; Landner, L. *Appl. Environ. Microbiol.* **1983**, *45*, 774.
- (11) DIN 38409. Beuth-Verlag GmbH: Berlin, 1985; Teil 14.
- (12) Hynning, P.-Å.; Remberger, M.; Neilson, A. H. *J. Chromatogr.* **1989**, *467*, 99.
- (13) Neilson, A. H.; Allard, A.-S.; Lindgren, C.; Remberger, M. *Appl. Environ. Microbiol.* **1987**, *53*, 2511.
- (14) Neilson, A. H.; Allard, A.-S.; Fischer, S.; Malmberg, M.; Viktor, T. *Ecotoxicol. Environ. Saf.* **1990**, *20*, 82.
- (15) Clark, W. M. *Oxidation-reduction potentials of organic systems*; The Williams and Wilkins Co.: Baltimore, MD, 1960.
- (16) Hart, W. G. *Org. Chem. Bull.* **1961**, *33*(3).
- (17) Dence, C. W.; Gupta, M. K.; Sarkanen, K. V. *Tappi* **1962**, *45*, 29.

Received for review April 8, 1991. Revised manuscript received June 24, 1991. Accepted June 28, 1991. Support from the Knut and Alice Wallenberg Foundation for funding toward purchase of the mass spectrometer is gratefully acknowledged.

Photodissolution of Iron Oxides. 3. Interplay of Photochemical and Thermal Processes in Maghemite/Carboxylic Acid Systems

Marta I. Litter, Erwin C. Baumgartner, Guillermo A. Urrutia, and Miguel A. Blesa*

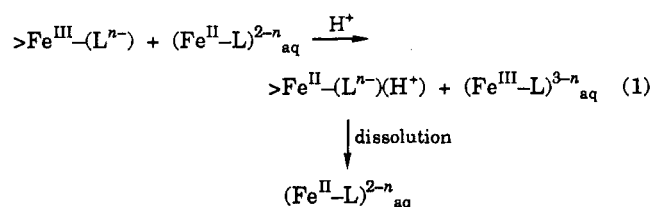
Departamento Química de Reactores, Comisión Nacional de Energía Atómica, Avenida del Libertador 8250, 1429 Buenos Aires, Argentina

■ Irradiation of γ -Fe₂O₃ suspensions in the presence of oxalate and EDTA results in a complex interplay between photochemical and thermal electron-transfer reactions. In the thermal dissolution, surface $>\text{Fe}^{\text{III}}\text{-L}$ complexes are slowly transferred by acid and reductive pathways until $\text{Fe}^{\text{II}}\text{-L}$ buildup in solution produces a strong acceleration. Irradiation accelerates the reaction by producing Fe^{2+} , heterogeneously by photolysis of the oxide surface complexes, and by homogeneous photolysis of aqueous $\text{Fe}^{\text{III}}\text{-L}$. This latter process is responsible for the acceleration in photodissolution rates brought about by the addition of $\text{Fe}^{3+}_{\text{aq}}$. Experimental results are reasonably fitted by the analytical solution of the simplified set of kinetic equations.

Introduction

The erosion of rocks and the dissolution of soils and sediments are sources for dissolved iron that is mobilized

in aquatic systems. These processes take place in the interface iron oxide/water, and it has been thoroughly documented (1) that dissolved ferrous ions greatly enhance the rates of incorporation of further iron [as iron(III)] to the aquatic medium; other reductants also dissolve iron oxides, this time as iron(II), in a process that is especially important in anoxic conditions (2-6) (eq 1; where $>$ denotes the lattice surface of the oxide).



As in many other environmentally important reactions, light may greatly influence the above thermal processes.

A series of papers (7-16) have described the photochemical dissolution of iron oxides, and similar behavior has been observed in the aquatic chemistry of manganese (17-19). Because of the role of iron oxides as photocatalysts (20, 21), the subject has also received increased interest in the last years in the field of materials science. By now, it seems clear that the primary light absorption act is the creation of $[e^-, h^+]$ pairs in the oxide, followed by h^+ and Fe^{II} transfer to solution when suitable reductants are present. These processes occur whenever surface states are created that trap electrons and become dissolution sites. The usual way to create surface states is by adsorption of complexing agents, such as thioglycolate (11, 12), citrate (9), and EDTA (15). These ligands further behave as sacrificial reductants that scavenge the holes created in the light absorption process. The overall stoichiometry of the photochemical reaction is therefore that of the reductive dissolution of the oxide by the organic anion.

All wavelengths able to excite charge-transfer components of the semiconductor absorption spectrum are able to produce significant photodissolution. Conversely, longer wavelengths, of energy below the absorption edge, are photochemically inactive (22).

Although these basic aspects are by now fairly well established, the kinetics of the ensuing photochemical dissolution has received much less attention. In an earlier paper (15), we described the photochemical dissolution of $\gamma\text{-Fe}_2\text{O}_3$ in the presence of EDTA. Only measurements at a single irradiation time were reported, and thus the complexities of the time dependence of the rate of dissolution were not explored. However, when the extent of photodissolution of an iron(III) oxide is appreciable, it is expected that thermal processes involving photoproduct dissolved Fe^{II} may become significant. The importance of dissolved ferrous ions in the photochemical dissolution of $\alpha\text{-FeOOH}$ in oxalic acid media was reported by Cornell and Schindler (14), who found an acceleratory rate of reaction later arrested by the formation of a coating of insoluble ferrous oxalate. Even this analysis falls short in the consideration of all the possible complexities involved, for instance, the homogeneous photolysis of $(Fe^{III}\text{-L})^n$ -complexes and the scavenging of photoproduct electrons by adsorbed Fe^{III} complexes.

In this paper we report a kinetic study on the photolysis of $\gamma\text{-Fe}_2\text{O}_3$ in the presence of oxalate and EDTA that demonstrates the existence of a complex interplay between photochemical and thermal electron-transfer reactions. For our experimental study, we chose acidic (pH 3-4) conditions rather than those of natural aquatic media, because this pH range optimizes the possibility of understanding that interplay and allows exploration of the changes brought about by changing the nature of the oxide. After this work had been essentially completed, Sulzberger and Siffert provided us with copies of their detailed analysis of the photolysis of hematite in oxalic acid solutions (2, 3, 23). In the present paper, we demonstrate that the general mechanism describing the complex reaction sequence can be analyzed quantitatively to derive rate constants. The rate values, calculated for our and Sulzberger's systems, can be used to characterize the relative reactivity of the various oxides and the influence of the environment on the reactivity.

Experimental Section

Maghemite ($\gamma\text{-Fe}_2\text{O}_3$) was a commercial sample and was the same as used previously (15). The average length of the acicular particles was $0.5\ \mu\text{m}$, aspect ratio 7/1, and the specific BET surface area of the solid was $25\ \text{m}^2\ \text{g}^{-1}$. Hematite ($\alpha\text{-Fe}_2\text{O}_3$) was also a commercial sample (Mal-

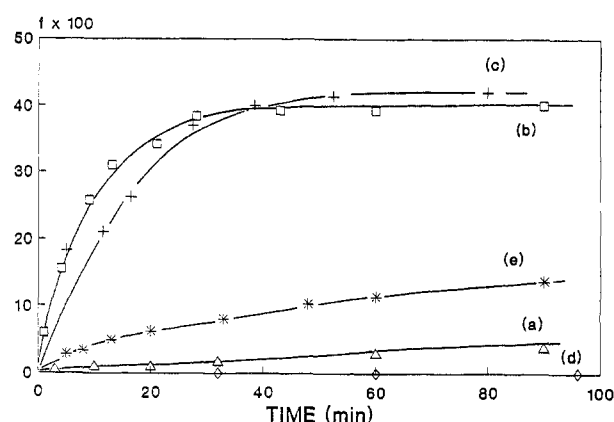


Figure 1. Iron fraction thermally dissolved from iron oxides by oxalic acid as a function of time: $[\gamma\text{-Fe}_2\text{O}_3] = 1\ \text{g}\ \text{dm}^{-3}$; $[\alpha\text{-Fe}_2\text{O}_3] = 2.55\ \text{g}\ \text{dm}^{-3}$; [oxalic acid] = $1.6 \times 10^{-2}\ \text{mol}\ \text{dm}^{-3}$; pH 4. Key: (a) $\gamma\text{-Fe}_2\text{O}_3$, 30 °C, $[Fe^{2+}] = 0$; (b) $\gamma\text{-Fe}_2\text{O}_3$, 70 °C, $[Fe^{2+}] = 0$; (c) $\gamma\text{-Fe}_2\text{O}_3$, 30 °C, $[Fe^{2+}] = 2.65 \times 10^{-4}\ \text{mol}\ \text{dm}^{-3}$; (d) $\alpha\text{-Fe}_2\text{O}_3$, 30 °C, $[Fe^{2+}] = 0$; (e) $\alpha\text{-Fe}_2\text{O}_3$, 30 °C, $[Fe^{2+}] = 2.65 \times 10^{-4}\ \text{mol}\ \text{dm}^{-3}$.

linkrodt). Its specific BET surface area was $9.8\ \text{m}^2\ \text{g}^{-1}$.

Reagents were of analytical purity or better and were used without further purification. Water was bidistilled in a quartz apparatus. Diluted H_2SO_4 or NaOH were used for pH adjustment.

Thermal kinetic experiments were carried out in a cylindrical beaker provided with a water jacket. In typical experiments, dissolution reactions were initiated by adding 50 mg of oxide to 50 cm^3 of a $1.6 \times 10^{-2}\ \text{mol}\ \text{dm}^{-3}$ oxalate solution at pH 4, previously thermostated at the desired temperature. In some experiments, the initial solution also contained $2.65 \times 10^{-4}\ \text{mol}\ \text{dm}^{-3}\ Fe^{2+}$. Periodically, samples of the magnetically stirred suspension were syringed into ca. 3 cm^3 of H_2O and filtered through a $0.2\text{-}\mu\text{m}$ pore-size membrane. Total iron was determined by the thioglycolate method (24). In some experiments, Fe^{2+} was independently determined by the *o*-phenanthroline method (25).

Photolysis experiments at 254 nm were carried out as previously described (15), using a germicidal lamp. Each sample was irradiated for a prefixed time and immediately filtered through a $0.2\text{-}\mu\text{m}$ pore-size membrane. In the filtered solution, total iron was determined by the already mentioned thioglycolate method (24), and formaldehyde by the chromotropic acid method (26).

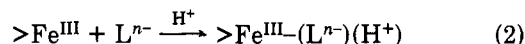
Two sets of experiments were carried out with a time interval of 9 months to check the importance of aging on the reactivities.

Absorbances were measured in a Metrolab 2500 spectrophotometer.

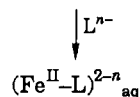
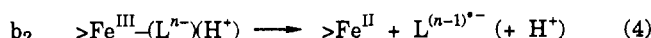
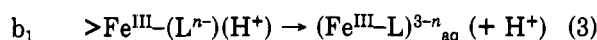
Results and Discussion

Thermal Dissolution in Oxalic Acid Media. Dissolution of maghemite at room temperature (30 °C) is very slow, as shown in Figure 1 (curve a). The reaction is greatly accelerated by either increasing the temperature to 70 °C (curve b) or by the addition of Fe^{2+} (curve c).

The mechanism of dissolution of iron oxides by carboxylates in acid media includes the following steps (27): (a) a fast preequilibrium step in which surface complexes $>Fe^{III}\text{-L}$ are formed through adsorption



(b) slow dissolution of the surface complex $>Fe^{III}\text{-L}$ through two parallel paths corresponding to acid and reductive dissolution, respectively



(c) a fast reductive reaction between $(\text{Fe}^{\text{II}}\text{L})^{2-n}$ complexes and Fe^{III} surface centers, conducive to a strong acceleration when $\text{Fe}^{2+}_{\text{aq}}$ reaches appropriate values (see eq 1 above).

In the case of magnetite, stages b and c are enhanced because, through all the dissolution processes (b_1 , b_2 , and c), constituent ferrous ions are also transferred to the solution alongside the reactive $>\text{Fe}^{\text{III}}$ centers. Typical sigmoidal dissolution profiles are predicted by this scheme and have been observed in a previous study of the dissolution of magnetite in oxalate solutions (4, 5). These sigmoidal f /time profiles could be fitted by a kinetic expression of the form

$$df/dt = R_0 + k[\text{Fe}^{2+}]S \quad (5)$$

where f is the fraction of the solid dissolved at time t , R_0 is a slow reaction rate, independent of $[\text{Fe}^{2+}]$, corresponding to process b, k is a specific reaction rate constant corresponding to step c, and $S = S_0(1-f)^{2/3}$ is the instantaneous surface area. The concentration of ferrous ion is assumed to be proportional to f .

In the absence of lattice Fe^{II} ions, as in hematite, only reaction b_2 contributes to the buildup of aqueous Fe^{2+} needed to trigger reaction c, and the overall observed rates are in general considerably lower; hence, higher temperatures are required. At 90 °C, the dissolution of hematite by EDTA is rather rapid, and the sigmoidal f/t profiles can be fitted (27) by expression 6:

$$df/dt = R_1(1-f)^{2/3} + k_T R_1 t(1-f)^{2/3} \quad (6)$$

where

$$k_T = k(m_0 S_0 / VM) \text{ and } R_1(1-f)^{2/3} = R_0$$

The first term accounts for the reductive dissolution by the carboxylate (reaction 4), and the second term corresponds to the process brought about by the ferrous carboxylate (reaction 1). Integrated eq 6 is quadratic in the time interval for which $f \ll 1$.

The data in Figure 1 fit well the above kinetic scheme and indicate a higher reactivity of maghemite (curves a and c) as compared to hematite (curves d and e). In the presence of added Fe^{2+} , the second term on the right-hand side of eq 5 is much larger than the first term, even at $t = 0$. Therefore, from the initial slope R_i of curve c ($5.67 \times 10^{-4} \text{ s}^{-1}$), and using eq 5 (see, however, ref 6), it is possible to calculate $k = R_i/[\text{Fe}^{2+}]_0 S_0 = 8.55 \times 10^{-6} \text{ dm}^3 \text{ mol}^{-1} \text{ cm}^{-2} \text{ s}^{-1}$. From the initial slope of curve e, the corresponding value for hematite is $7.05 \times 10^{-7} \text{ dm}^3 \text{ mol}^{-1} \text{ cm}^{-2} \text{ s}^{-1}$. Curve b is indicative of a fast thermal production of Fe^{2+} through pathway b_2 at 70 °C, in agreement with the results on nickel ferrite (28). In some experiments at 70 °C, measurements of Fe^{2+} in solution gave positive results, indicating that reductive dissolution is indeed taking place; the results were, however, too erratic to evaluate the quantitative contribution of (b_2). On the other hand, the contribution of (b_2) to dissolution of maghemite at 30 °C (curve a) may be very low (cf. ref 23).

Photochemical Dissolution in Oxalic Acid. In Figure 2, curve b shows the buildup of iron in solution in a suspension of maghemite in oxalate at pH 4 and 30 °C under irradiation at 254 nm. Comparison with curve a indicates the enhancement of dissolution by irradiation.

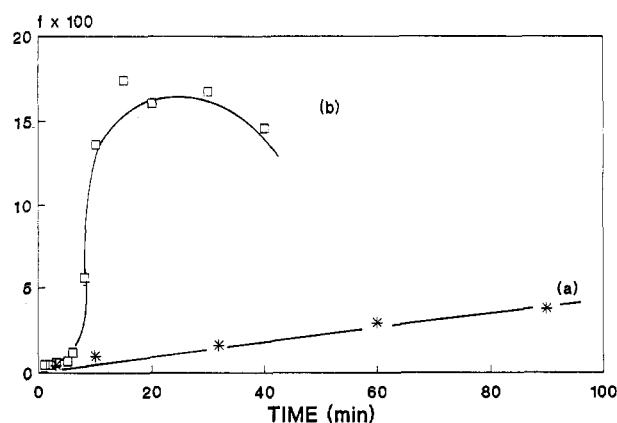


Figure 2. Comparison of thermal (a) and 254-nm photochemical (b) dissolution profiles of $\gamma\text{-Fe}_2\text{O}_3$ in oxalic acid: $[\gamma\text{-Fe}_2\text{O}_3] = 1 \text{ g dm}^{-3}$; $[\text{oxalic acid}] = 1.6 \times 10^{-2} \text{ mol dm}^{-3}$; pH 4; 30 °C.

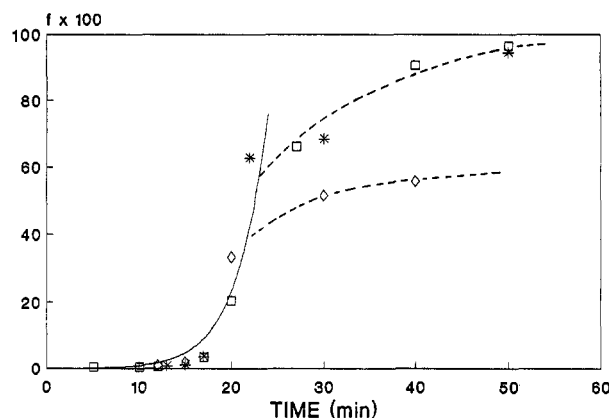
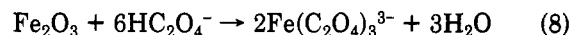
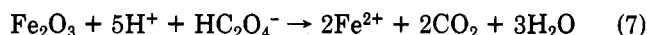


Figure 3. 254-nm photodissolution profiles of $\gamma\text{-Fe}_2\text{O}_3$ in EDTA at 30 °C and pH 3: $[\gamma\text{-Fe}_2\text{O}_3] = 1 \text{ g dm}^{-3}$. Key: (\diamond) $[\text{EDTA}] = 1 \times 10^{-2}$; ($*$) $[\text{EDTA}] = 2 \times 10^{-2}$; (\square) $[\text{EDTA}] = 4 \times 10^{-2} \text{ mol dm}^{-3}$. Solid curve was obtained through the analytical solution of eqs 20 and 21, using the following parameters: $k_1 = 5.0 \times 10^{-11} \text{ mol dm}^{-3} \text{ s}^{-1}$; $k'_2 = 5.0 \times 10^{-6} \text{ s}^{-1}$; $k_T = 5.5 \text{ s}^{-1}$.

As opposed to the thermal process at 70 °C (curve b in Figure 1), the reaction is arrested at lower fractions of dissolution. The formation of insoluble $\beta\text{-FeC}_2\text{O}_4 \cdot 2\text{H}_2\text{O}$ is observed visually, in agreement with the report by Cornell and Schindler (14). In addition, a large positive pH shift from 4 to 6.4 is observed. The stoichiometry of the two possible processes leading to dissolution are represented by eqs 7 and 8; the former is more important under light, requires more protons than the latter, and accounts for the shift in pH during the photochemical process.



The photochemical production of Fe^{2+} at the interface gives rise to a supersaturation of $\beta\text{-FeC}_2\text{O}_4 \cdot 2\text{H}_2\text{O}$ that upon surface precipitation might prevent further photolysis; more importantly, the rise in pH arrests the dissolution, either thermal or photochemical (1, 15). Because of these complications, the interpretation of the mechanism of the photochemical process becomes involved and it is better to analyze this aspect and the observed sigmoidal profile in the system $\gamma\text{-Fe}_2\text{O}_3/\text{EDTA}$ discussed below.

Photochemical Dissolution in EDTA Media. The thermal dissolution of iron oxides in EDTA has been studied previously (6, 27). Dissolution is slow at room temperature and can be accelerated only by increasing the temperature or by the addition of Fe^{2+} . Equation 6 has

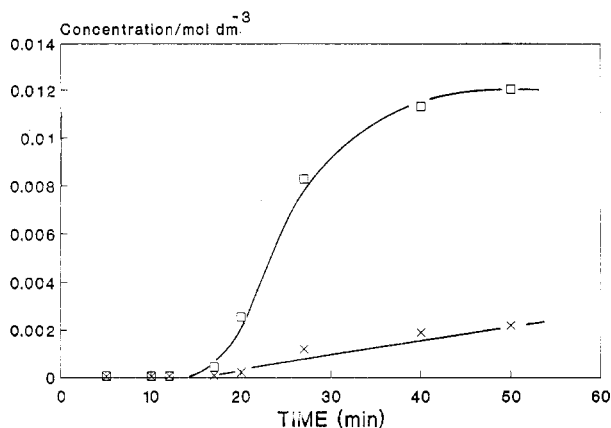


Figure 4. Comparison of the production rates of iron (\square) and formaldehyde (\times) in the 254-nm photodissolution of γ - Fe_2O_3 (1 g dm^{-3}) in EDTA ($4 \times 10^{-2} \text{ mol dm}^{-3}$) at pH 3.

been used to describe the kinetics of the thermal reaction of hematite and EDTA at 90°C (27). Figure 3 shows the autoacceleratory dissolution profiles of suspensions of maghemite at three different EDTA concentrations at pH 3 under UV irradiation. The influence of EDTA concentration on either the length of the induction period or the slope of the fast reaction is not large. Ligand concentration noticeably influences the total amount of dissolved iron. This result is simply a consequence of the stoichiometry of the reaction and reflects the depletion of free EDTA under the conditions used in the photolysis experiments. At longer irradiation times, a gentle increase in dissolution fraction is observed in the three cases, the slope being slightly more pronounced at higher concentrations. This secondary effect can be attributed to the photolysis of dissolved Fe^{III} -EDTA (29, 30). The stoichiometry of the homogeneous photolysis (eq 9) allows for the recovery of



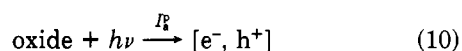
ferrous ions, where L is a degradation product of EDTA, such as iminodiacetic acid. The fast thermal reaction with the remaining solid brings about further dissolution.

Photoproducted formaldehyde was also measured. In Figure 4, the production rates of total iron and formaldehyde are compared.

In the thermal reactions, addition of Fe^{3+} does not influence the rate to a large extent, unless it is added in concentrations high enough to scavenge appreciable amounts of EDTA, thus arresting the reaction (6). In contrast, Fe^{3+} appreciably enhances the photochemical reaction. Figure 5 shows the results; the influence on the induction period is noticeable and becomes more evident at higher concentrations of Fe^{3+} . The suppression of the induction period by Fe^{3+} is a very peculiar and important feature of the photochemical reaction.

The characteristics of the dissolution process triggered by light, shown in Figures 2-5, can be adequately described by the following set of reactions.

(a) Primary photochemical production of electron-hole pairs



where I_a^p is the total light intensity absorbed by the particles.

(b) Reactions of $[e^-, h^+]$ at the surface. (b₁) recombination:

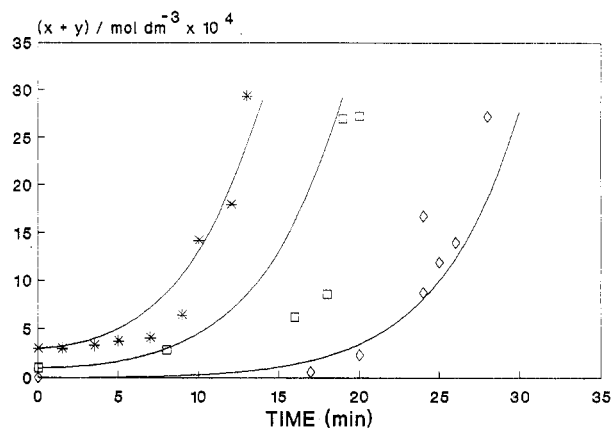
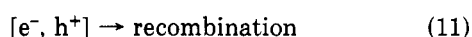
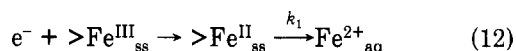
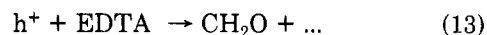


Figure 5. 254-nm photodissolution profiles of γ - Fe_2O_3 in EDTA at 30°C and pH 3 in the presence of added Fe^{3+} : $[\gamma\text{-Fe}_2\text{O}_3] = 0.5 \text{ g dm}^{-3}$; $[\text{EDTA}] = 2 \times 10^{-2} \text{ mol dm}^{-3}$. Key: (\diamond) $[\text{Fe}^{3+}] = 0$; (\square) $[\text{Fe}^{3+}] = 1 \times 10^{-4}$; ($*$): $[\text{Fe}^{3+}] = 3 \times 10^{-4} \text{ mol dm}^{-3}$. Solid curves were obtained through the analytical solutions of eqs 20 and 21, using the following parameters: $k_1 = 3.3 \times 10^{-11} \text{ mol dm}^{-3} \text{ s}^{-1}$, $k'_2 = 3.2 \times 10^{-6} \text{ s}^{-1}$, and $k_T = 3.8 \text{ s}^{-1}$.

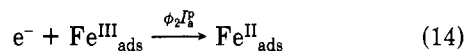
(b₂) photodissolution controlled by the rate of phase transfer of e^- trapped as Fe^{II} in surface states (ss):



where $k_1 = \phi_1 I_a^p$ (ϕ_1 is the quantum yield of Fe^{2+} production in reaction 12) is the rate of production of dissolved Fe^{2+} due to the photochemical process. Holes oxidize adsorbed EDTA:



(The overall stoichiometry is affected by the secondary reactions between other Fe^{III} centers and the organic radicals arising from the oxidation of EDTA.) (b₃) trapping of e^- by adsorbed Fe^{III} -EDTA species:

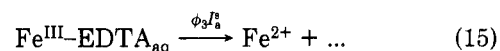


where $\phi_2 I_a^p = k_2 [\text{Fe}^{\text{III}}]_{\text{ads}}$. If $[\text{Fe}^{\text{III}}]_{\text{ads}}$ is proportional through the adsorption constant K to the Fe^{III} bulk concentration, $k_2 [\text{Fe}^{\text{III}}]_{\text{ads}} = k_2 K [\text{Fe}^{\text{III}}]$ and $\phi_2 I_a^p = k_2 K [\text{Fe}^{\text{III}}]$; i.e., first-order kinetics results for conditions of low quantum yield ϕ_2 .

Again, holes oxidize adsorbed EDTA. This process may be viewed as the catalysis by the oxide of the photodegradation of aqueous Fe^{III} -EDTA complexes.

(c) Thermal dissolution of the oxide by dissolved Fe^{II} -EDTA complexes (eq 1), characterized by k_T .

(d) Homogeneous photolysis of aqueous Fe^{III} -EDTA:



where I_a^s is the total light intensity absorbed by dissolved Fe^{III} -EDTA.

The values of I_a^p and I_a^s are given by

$$I_a^p = I_0 \frac{\sigma_p c_p}{\sigma_p c_p + \epsilon_y y} [1 - e^{-(\sigma_p c_p + \epsilon_y y)l}] \quad (16)$$

$$I_a^s = I_0 \frac{\epsilon_y y}{\sigma_p c_p + \epsilon_y y} [1 - e^{-(\sigma_p c_p + \epsilon_y y)l}] \quad (17)$$

where σ_p is the effective particle cross section for light absorption, c_p is the particle concentration, ϵ_y and y are the molar extinction coefficient of Fe^{III} -L in solution and the instantaneous molar concentration, respectively, and l is the optical path length.

This set of equations may be used to predict the rates of increase of Fe^{2+} , Fe^{3+} , and CH_2O concentrations in so-

lution. Some assumptions can be made to simplify the problem: (1) The rate of thermal dissolution (eq 1) is proportional to the concentration of Fe^{2+} in solution and to the instantaneous surface area S . (2) The instantaneous surface area is proportional to $(1-f)^n$, f being the fraction of solid dissolved at time t , and n being $2/3$ for isometric tridimensional particles or $1/2$ for acicular particles. (3) The changes in rate due to EDTA depletion are not taken into account.

Denoting the instantaneous molar concentration of Fe^{2+} in solution by x , the ensuing coupled differential equations are

$$dx/dt = \phi_1 I_a^p + \phi'_2 I_a^p y + \phi_3 I_a^s \quad (18)$$

$$dy/dt = -\phi_3 I_a^s - \phi'_2 I_a^p y + k_T [1 - (f_y + f_x)]^n x \quad (19)$$

where $\phi'_2 y = \phi_2$, $f_y = y/(x+y)_\infty$, and $f_x = x/(x+y)_\infty$.

These equations can be solved numerically, using the boundary conditions $x_0 = y_0 = 0$ and $x_\infty = (m_0/MV)$, $y_\infty = 0$, where m_0 , M , and V are the initial oxide mass, its molar mass, and the solution volume, respectively. It is more instructive, however, to center the analysis on a simple limiting case, amenable to analytical solution. At low conversions, the last bracket in eq 19 is simply 1. If, furthermore, $\sigma_p c_p \gg \epsilon_y y$, (i.e., $I_a^p \simeq I_0$), and ϕ_2 is very low, the resulting equations are of the form

$$dx/dt = k_1 + k'_2 y \quad (20)$$

$$dy/dt = -k'_2 y + k_T x \quad (21)$$

where $k_1 = \phi_1 I_0$ and $k'_2 = (K^{-1} \phi'_2 + \phi_3 \alpha) I_0$; $\alpha = \epsilon_y / \sigma_p c_p$.

Equations 20 and 21 are easily solved by Laplace transforms, using the boundary conditions $x_0 = 0$ and $y_0 = 0$. The plot for calculated fraction of dissolution vs time is shown in Figure 3 together with the experimental data; adequate values of k_1 , k'_2 , and k_T were chosen to fit these data. The parameter k_1 is most important in defining the length of the induction period in the absence of added Fe^{II} or Fe^{III} . The sharp increase in dissolution fraction once the induction period is overcome is defined by the values of k'_2 and k_T . The best fit of the whole set of experimental data of Figure 3 was achieved with $k_1 = 5.0 \times 10^{-11} \text{ mol dm}^{-3} \text{ s}^{-1}$, $k'_2 = 5.0 \times 10^{-6} \text{ s}^{-1}$, and $k_T = 5.5 \text{ s}^{-1}$. The value of k'_2 is reasonable in the sense that $k'_2 y < I_0$ in the early stages of reaction. The value of k_T is analyzed below, although it should be noted that the dependence of the rate of thermal dissolution on the concentration of ferrous complexes is still an open question. A more explosive growth ensues if $x^{n'}$ is substituted for x in eq 21 ($n' > 1$), and the partial order n' can in fact take different values under various experimental conditions; for the rather simple case of chemisorption of Fe^{II} -EDTA, n' may vary monotonously from 1 to 0 as $[\text{Fe}^{\text{II}}$ -EDTA] increases. Also, the buildup of Fe^{II} in the interface brought about by dissolution is not necessarily equivalent to the addition of ferrous salts: the dependence on f and on $[\text{Fe}^{2+}]$ may not be identical. Any attempt to model these effects introduces necessarily new fitting parameters and seems unwarranted on the basis of the limited available evidence.

The influence of Fe^{II} scavengers can also be modeled adequately. As k_1 represents the buildup of Fe^{II} , it is in fact smaller than the actual rate of dissolution during the induction period (31, 32). If oxidants are present, eqs 20 and 21 are modified in the simplest case to

$$dx/dt = k_1 - k_{ox}[\text{O}]x + k'_2 y \quad (22)$$

$$dy/dt = -k'_2 y + (k_{ox}[\text{O}] + k_T)x \quad (23)$$

where $[\text{O}]$ is the concentration of oxidant and k_{ox} the second-order rate constant of the oxidation of Fe^{II} . Massive dissolution may be arrested as long as $k_{ox}[\text{O}]$ is

large enough to prevent x from reaching a value adequate to trigger thermal dissolution. Under certain conditions, however, depletion of the oxidant shall take place. In particular, during magnetite dissolution, an anoxic environment can be created by the dissolution reaction itself, and oxygen may not prevent dissolution; large k_1 and k'_2 values produce the same effect. On the other hand, if k_1 is small, oxygen is likely to arrest totally the thermal dissolution. This analysis explains the different importance of dissolved oxygen under Sulzberger's (2) experimental conditions and our own.

Furthermore, it is interesting to compare the time behavior of $[\text{Fe}_{\text{aq}}]_{\text{T(otal)}}$ and $[\text{Fe}^{2+}_{\text{aq}}]$. Although we have not measured $[\text{Fe}^{2+}_{\text{aq}}]$, the stoichiometry of the reaction producing Fe^{2+} requires that CH_2O also be produced (eq 9), in a ratio $n_{\text{Fe}^{2+}}/n_{\text{CH}_2\text{O}} = 2$; thus, the profiles $[\text{CH}_2\text{O}]$ vs t are equivalent to profiles $1/2[\text{Fe}^{\text{II}}]$ vs t . Figure 4 shows a clear time dephasing of the production of total Fe_{aq} and CH_2O as a result of the thermal dissolution process that does not produce CH_2O . In either the simplified set of eqs 20 and 21 or in the more complex set 18 and 19, homogeneous photolysis of Fe^{III} -EDTA is lumped together with the heterogeneous equivalent process, i.e., the process mediated by the absorption of light by the oxide "catalyst" and the ensuing transfer of e^- and h^+ to adsorbed Fe^{III} and EDTA, respectively. Our experiments have been carried out under conditions where $I_0 \simeq I_a^p + I_a^s$; while absorption by the solid is prevalent at low conversions, the contribution to the rate of Fe^{2+} production by homogeneous photolysis is always important, because $\phi_3 \simeq 0.2$ (25) is certainly much larger than ϕ'_2 . At longer times I_a^p becomes comparable with I_a^s and homogeneous photolysis is the main source of Fe^{II} ; under these conditions, the rate of production of Fe^{II} becomes rather insensitive to $[\text{Fe}^{\text{III}}]$ because of the "saturation" of I_a^s (see eq 17). The amount of CH_2O produced during photodissolution is very small and subject to a high relative error, which precludes a good estimation of the (small) ratio $\text{Fe}^{2+}/\text{Fe}_T$ during the early stages of reaction. It is only when homogeneous photolysis of Fe^{III} becomes dominant that a substantial buildup of CH_2O is observed. From Figure 4 it is clear that homogeneous photolysis is the main source of formaldehyde because the slope of the curve ($1.2 \times 10^{-6} \text{ mol dm}^{-3} \text{ s}^{-1}$) is in reasonable agreement with the calculated value of $\phi_3 I_0 = 3.9 \times 10^{-6} \text{ mol dm}^{-3} \text{ s}^{-1}$, calculated from literature data for ϕ_3 (25).

Addition of Fe^{III} salts changes the boundary condition $y_0 = 0$ to $y_0 = c$; analogously, addition of Fe^{2+} yields $x_0 = b$. Solving the equations for the case of addition of Fe^{3+} , the profiles shown in Figure 5 are obtained, in fair agreement with the experimental results. In the presence of added Fe^{III} , light absorption by the solid becomes less important; at high y_0 values, the process is simply the coupling of homogeneous photolysis and heterogeneous thermal reaction (i.e., k_1 becomes negligible). In agreement, CH_2O is produced from the beginning (see Figure 6). The parameter k_1 is sensitive in principle to experimental conditions such as the presence of traces of air or lack of stability of light intensity. In addition, all three constants k_1 , k'_2 , and k_T are sensitive to the previous history of the oxide sample. In our systems, k_1 was found to decrease for sets of experiments carried out with large time intervals in between: its value in the early experiments depicted in Figure 3 is $5.0 \times 10^{-11} \text{ mol dm}^{-3} \text{ s}^{-1}$, as opposed to the value of $3.3 \times 10^{-11} \text{ mol dm}^{-3} \text{ s}^{-1}$ for the later experiments included in Figure 5. Similar trends, i.e., a decrease of ca. 40%, were observed for k'_2 and k_T . It is unlikely that single values of the constants can be ascribed

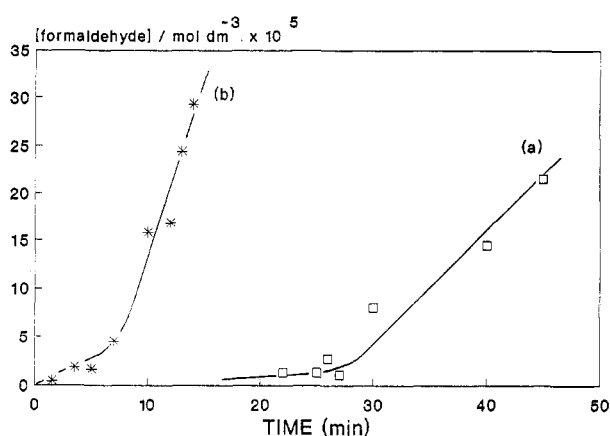


Figure 6. Rates of production of formaldehyde during the 254-nm photodissolution of $\gamma\text{-Fe}_2\text{O}_3$ in EDTA at 30 °C and pH 3: $[\gamma\text{-Fe}_2\text{O}_3] = 0.5 \text{ g dm}^{-3}$; $[\text{EDTA}] = 2 \times 10^{-2} \text{ mol dm}^{-3}$. Key: (a) $[\text{Fe}^{3+}] = 0$; (b) $[\text{Fe}^{3+}] = 3 \times 10^{-4} \text{ mol dm}^{-3}$. The data correspond to experiments of Figure 5.

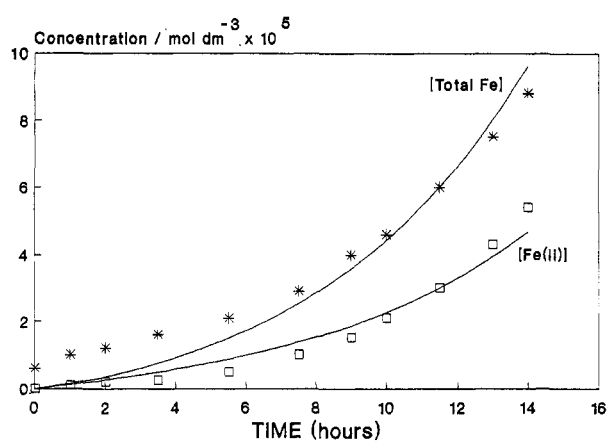


Figure 7. Fitting of the data of Sulzberger et al. (2, 3, 23) for the 375-nm photodissolution of hematite in the presence of oxalate at pH 3: $[\alpha\text{-Fe}_2\text{O}_3] = 0.5 \text{ g dm}^{-3}$; $[\text{oxalate}] = 3.3 \times 10^{-3} \text{ mol dm}^{-3}$. Solid lines were obtained by solving eqs 20 and 21, using the following parameters: $k_1 = 3.6 \times 10^{-10} \text{ mol dm}^{-3} \text{ s}^{-1}$, $k'_2 = 3.9 \times 10^{-5} \text{ s}^{-1}$, and $k_T = 9.7 \times 10^{-5} \text{ s}^{-1}$.

to a given iron oxide, because of its sensitiveness to aging.

Siffert and Sulzberger (2, 23) carried out a detailed study of the photochemical dissolution of hematite in the presence of oxalate under N_2 atmosphere and proposed a similar reaction sequence to describe qualitatively their data, although they postulated a Langmuir-type dependence of the thermal reaction rate on dissolved $[\text{Fe}^{\text{II}}]$ (cf. eq 41 in ref 2). In addition to the different ligand, and the use of N_2 atmosphere, there were other important differences in their experimental conditions: (a) very long reaction times (several hours); (b) low degrees of dissolution (typically, $f < 0.1$), even in the presence of added Fe^{II} . The large difference in rate is due essentially to the lower reactivity of $\alpha\text{-Fe}_2\text{O}_3$ as compared to $\gamma\text{-Fe}_2\text{O}_3$. It is therefore of interest to check the applicability of the equation derived here to the data of Siffert and Sulzberger. Figure 7 shows that $k_1 = 3.6 \times 10^{-10} \text{ mol dm}^{-3} \text{ s}^{-1}$, $k'_2 = 3.9 \times 10^{-5} \text{ s}^{-1}$, and $k_T = 9.7 \times 10^{-5} \text{ s}^{-1}$ fit their data reasonably well. Their $[\text{Fe}^{\text{II}}]$ vs time curve is also well reproduced; the larger k'_2/k_T ratio accounts for the lack of buildup of substantial amounts of Fe^{III} in solution. The differences in oxide, complexant, and experimental conditions preclude any attempt to compare Siffert and Sulzberger's k_1 and k'_2 values with ours; the valid conclusion, however, remains that the extent of dissolution under light is governed essentially by the thermal dissolution rate constant k_T , which

is 10^4 larger for $\gamma\text{-Fe}_2\text{O}_3/\text{EDTA}$ than for $\alpha\text{-Fe}_2\text{O}_3/\text{oxalate}$ (2, 20, 33). This large difference is certainly associated with the different oxide properties, rather than with the aggressiveness of the ligand.

Acknowledgment is made to Profs. W. Stumm and M. Grätzel and to Drs. R. Cornell, B. Sulzberger, and J. Hering for helpful discussions. M.I.L. and M.A.B. are members of CONICET.

Glossary

c_p	oxide particle concentration (g dm^{-3})
f	fraction of total iron dissolved (dimensionless)
f_x	fraction of Fe^{II} dissolved (dimensionless)
f_y	fraction of Fe^{III} dissolved (dimensionless)
h	Planck constant, $6.63 \times 10^{-34} \text{ J s}$
I_a^p	light intensity absorbed by the suspended oxide particles per unit solution volume (einstein $\text{s}^{-1} \text{ dm}^{-3}$)
I_a^s	light intensity absorbed by $(\text{Fe}^{\text{III}}\text{-EDTA})_{\text{aq}}$ per unit solution volume (einstein $\text{s}^{-1} \text{ dm}^{-3}$)
I_0	total incident light intensity per unit solution volume (einstein $\text{s}^{-1} \text{ dm}^{-3}$)
k	rate constant for the thermal dissolution brought about by dissolved ferrous ions (eq 5) ($\text{dm}^3 \text{ mol}^{-1} \text{ cm}^2 \text{ s}^{-1}$)
k_T	rate constant for the thermal dissociation brought about by dissolved ferrous ions (eq 6) (s^{-1}). $k_T = k(m_0 S_0 / MV)$
k_1	rate of production of dissolved Fe^{2+} due to the photochemical process (eq 12) ($\text{mol dm}^{-3} \text{ s}^{-1}$)
k_2	rate constant for the reaction of adsorbed Fe^{III} with e^- , which yields Fe^{II} (eq 14) (s^{-1})
k'_2	composite rate constant that embodies the heterogeneous and homogeneous photoproduction of Fe^{II} from Fe^{III} (s^{-1})
k_{ox}	second-order rate constant for the oxidation of Fe^{II} (eqs 22 and 23) ($\text{mol}^{-1} \text{ dm}^3 \text{ s}^{-1}$)
K	adsorption affinity of Fe^{III} , defined as $[\text{Fe}^{\text{III}}]_{\text{ads}} / [\text{Fe}^{\text{III}}]_{\text{bulk}}$ (dimensionless)
l	optical path length (cm)
m_0	initial oxide mass (g)
M	molar mass of the iron oxide (g mol^{-1})
n	geometric parameter related to the shape of oxide particles (dimensionless)
n'	partial order for Fe^{2+} in the thermal dissolution (dimensionless)
R_0	reaction rate characterizing the slow leaching of Fe^{II} from the oxide (eq 5) (s^{-1})
R_1	initial value of R_0 (for $f = 0$) (eq 6) (s^{-1})
R_i	experimental initial reaction rate (curves c and e in Figure 1) (s^{-1}); $R_i = k[\text{Fe}^{2+}]_0 S_0$
S	instantaneous surface area (cm^2)
S_0	initial surface area (cm^2)
t	reaction time (s)
V	solution volume (dm^3)
x	instantaneous $\text{Fe}^{2+}_{\text{aq}}$ molar concentration (mol dm^{-3})
x_0	initial $\text{Fe}^{2+}_{\text{aq}}$ molar concentration (mol dm^{-3})
x_{∞}	final $\text{Fe}^{2+}_{\text{aq}}$ molar concentration (mol dm^{-3})
y	instantaneous $\text{Fe}^{3+}_{\text{aq}}$ molar concentration (mol dm^{-3})
y_0	initial $\text{Fe}^{3+}_{\text{aq}}$ molar concentration (mol dm^{-3})
y_{∞}	final $\text{Fe}^{3+}_{\text{aq}}$ molar concentration (mol dm^{-3})
α	fraction of incident light absorbed by dissolved Fe^{III} , per unit $[\text{Fe}^{\text{III}}]$. At low concentrations, $\alpha = \epsilon_y / \sigma_p c_p$ ($\text{mol}^{-1} \text{ dm}^3$)
ϵ_y	molar extinction coefficient for $(\text{Fe}^{\text{III}}\text{-EDTA})_{\text{aq}}$ ($\text{mol}^{-1} \text{ dm}^2$)
ϕ_1	quantum yield of Fe^{II} production from surface Fe^{III} (eq 12)
ϕ_2	quantum yield of Fe^{II} production from adsorbed Fe^{III} (eq 14)
ϕ'_2	value of ϕ_2 when $[\text{Fe}^{\text{III}}] = 1 \text{ mol dm}^{-3}$ ($\phi'_2 = \phi_2 / [\text{Fe}^{\text{III}}]$)

ϕ_3 quantum yield of Fe^{2+} production by homogeneous photolysis of $\text{Fe}^{\text{III}}\text{-EDTA}$ (eq 15)
 σ_p effective oxide particle cross section for light absorption ($\text{dm}^2 \text{g}^{-1}$)
 ν frequency (s^{-1})

Registry No. EDTA, 60-00-4; maghemite, 12134-66-6; oxalic acid, 144-62-7.

Literature Cited

- (1) Blesa, M. A.; Regazzoni, A. E.; Maroto, A. J. G. *Mater. Sci. Forum* 1988, 29, 31-98.
- (2) Sulzberger, B. In *Aquatic Chemical Kinetics*; Stumm, W., Ed.; Wiley Interscience: New York, 1990.
- (3) Sulzberger, B.; Suter, D.; Siffert, C.; Banwart, S.; Stumm, W. *Mar. Chem.* 1989, 28, 127-144.
- (4) Baumgartner, E.; Blesa, M. A.; Marinovich, H. A.; Maroto, A. J. G. *Inorg. Chem.* 1983, 22, 2224-2226.
- (5) Blesa, M. A.; Marinovich, H. A.; Baumgartner, E. C.; Maroto, A. J. G. *Inorg. Chem.* 1987, 26, 3713-3717.
- (6) Borghi, E. B.; Regazzoni, A. E.; Maroto, A. J. G.; Blesa, M. A. *J. Colloid Interface Sci.* 1989, 130, 299-310.
- (7) Cunningham, K. M.; Goldberg, M. C.; Weiner, E. R. *Photochem. Photobiol.* 1985, 41, 409-416.
- (8) Stramel, R. D.; Thomas, J. K. *J. Colloid Interface Sci.* 1986, 110, 121-129.
- (9) Waite, T. D.; Morel, F. M. M. *J. Colloid Interface Sci.* 1984, 102, 121-137.
- (10) Waite, T. D.; Morel, F. M. M. *Environ. Sci. Technol.* 1984, 18, 860-868.
- (11) Waite, T. D.; Torikov, A.; Smith, J. D. *J. Colloid Interface Sci.* 1986, 112, 412-420.
- (12) Waite, T. D.; Torikov, A. *J. Colloid Interface Sci.* 1987, 119, 228-235.
- (13) Faust, B. C.; Hoffmann, M. R. *Environ. Sci. Technol.* 1986, 20, 943-948.
- (14) Cornell, R. M.; Schindler, P. W. *Clays Clay Miner.* 1987, 35, 347-352.
- (15) Litter, M. I.; Blesa, M. A. *J. Colloid Interface Sci.* 1988, 125, 679-687.

- (16) Cunningham, K. M.; Goldberg, M. C.; Weiner, E. R. *Environ. Sci. Technol.* 1988, 22, 1090-1097.
- (17) Sunda, W. G.; Huntsman, S. A.; Harvey, G. R. *Nature (London)* 1983, 301, 234-236.
- (18) Stone, A. T.; Morgan, J. J. *Environ. Sci. Technol.* 1984, 18, 617-624.
- (19) Waite, T. D.; Wrigley, I. C.; Szymczak, R. *Environ. Sci. Technol.* 1988, 22, 778-785.
- (20) Leland, J. K.; Bard, A. J. *J. Phys. Chem.* 1987, 91, 5076-5083.
- (21) (a) Kormann, C.; Bahnemann, D. W.; Hoffmann, M. R. *J. Photochem. Photobiol.* 1989, 48A, 161-169. (b) Faust, B. C.; Hoffmann, M. R.; Bahnemann, D. W. *J. Phys. Chem.* 1989, 93, 6371-6381.
- (22) Litter, M. I.; Blesa, M. A. *Can. J. Chem.* 1990, 68, 728-730.
- (23) Siffert, C. Ph.D. Thesis, ETH Zurich, Switzerland, 1989.
- (24) (a) Leussing, D. L.; Kolthoff, I. M. *J. Am. Chem. Soc.* 1953, 75, 3904-3911. (b) Leussing, D. L.; Newman, L. *J. Am. Chem. Soc.* 1956, 78, 552-556.
- (25) Tamura, H.; Goto, K.; Yotsuyanagi, T.; Nagayama, M. *Talanta* 1974, 21, 314-317.
- (26) Bricker, C. E.; Johnson, H. R. *Ind. Eng. Chem., Anal. Ed.* 1945, 17, 400-402.
- (27) Torres, R.; Blesa, M. A.; Matijevic, E. *J. Colloid Interface Sci.* 1990, 134, 475-485.
- (28) Sellers, R. M.; Williams, W. J. *Faraday Discuss. Chem. Soc.* 1984, 77, 265-274.
- (29) Carey, J. H.; Langford, C. H. *Can. J. Chem.* 1973, 51, 3665-3670.
- (30) Natarajan, P.; Endicott, J. F. *J. Phys. Chem.* 1973, 77, 2049-2054.
- (31) Regazzoni, A. E.; Blesa, M. A. *Langmuir* 1991, 7, 473-478.
- (32) Borghi, E. B.; Morando, P. J.; Blesa, M. A. *Langmuir*, in press.
- (33) Litter, M. I.; Blesa, M. A. *Can. J. Chem.*, submitted.

Received for review October 4, 1990. Revised manuscript received March 6, 1991. Accepted June 14, 1991. Partial support from CONICET and CICPBA are gratefully acknowledged.

Competitive Actinide Interactions in Colloidal Humic Acid-Mineral Oxide Systems

Luca Righetto,[†] Giovanni Bidoglio,^{*‡} Giovanna Azimonti,[†] and Ignazio R. Bellobono[†]

Commission of the European Communities, Joint Research Centre, Environment Institute, I-21020 Ispra (Va), Italy, and Dipartimento di Chimica Fisica ed Elettrochimica, Università di Milano, Via Golgi 19, I-20133 Milan, Italy

■ The adsorption behavior of americium, thorium, neptunium, and plutonium was investigated in multicomponent systems containing γ -alumina or amorphous silica as model inorganic particles and polydispersed humic acid (HA) colloids isolated from an organic-rich clay formation. The sorption selectivity of the actinide ions on bare mineral oxide particles can be explained on the basis of the hard-soft Lewis acid-base behavior. Competition experiments using HA indicated that the extent of actinide adsorption depends on the coordinating strengths of HA on the surface and in the solution.

Introduction

The underground disposal of nonexploitable by products from the nuclear industry has been identified as an ap-

propriate disposal strategy in many countries (1). The safety aspects of this choice can only be demonstrated indirectly through predictive modeling and from a broad range of experimental research activities (2). These should identify physicochemical processes that may lead to the over- or underestimation of risks.

Although the significance of humic (HA) and fulvic (FA) acids to biogeochemical processes in water environments has long been recognized (3-5), knowledge of their interactions with radionuclides in multicomponent systems in the presence of solid adsorbents is relatively limited (6-11). The radionuclides potentially released from nuclear waste matrices may sorb on particulate matter coming from the degradation of the waste packages and on natural colloids present in the leaching groundwater. The aim of this work was to investigate the influence of natural organic substances on Am, Th, Np, and Pu adsorption on selected hydrous mineral oxides. Am, Th, and Np were chosen as valence analogues for other tri-, tetra-, and pentavalent actinides. Pu, instead, was selected because it can exist

[†]Università di Milano.

[‡]Commission of the European Communities, Joint Research Centre.